



Power Electronic Systems  
Laboratory

© 2015 IEEE

Proceedings of the 41th Annual Conference of the IEEE Industrial Electronics Society (IECON 2015), Yokohama, Japan, November 9-12, 2015

## **Analysis and Power Scaling of a Single-Sided Linear Induction Machine for Energy Harvesting**

M. Flankl,  
A. Tüysüz,  
J. W. Kolar

This material is published in order to provide access to research results of the Power Electronic Systems Laboratory / D-ITET / ETH Zurich. Internal or personal use of this material is permitted. However, permission to reprint/republish this material for advertising or promotional purposes or for creating new collective works for resale or redistribution must be obtained from the copyright holder. By choosing to view this document, you agree to all provisions of the copyright laws protecting it.



Eidgenössische Technische Hochschule Zürich  
Swiss Federal Institute of Technology Zurich

# Analysis and Power Scaling of a Single-Sided Linear Induction Machine for Energy Harvesting

Michael Flankl, Arda Tüysüz and Johann W. Kolar  
Power Electronic Systems Laboratory  
Swiss Federal Institute of Technology (ETH Zurich),  
Physikstrasse 3  
8092 Zurich, Switzerland

**Abstract**— Although Single-Sided Linear Induction Machines (SLIMs) have been analyzed and tested intensively as prime movers for different applications in literature, their application for energy harvesting has not been studied rigorously. This paper investigates the use of SLIMs for watt-range energy harvesting from a moving steel body with smooth surface (solid steel secondary) in order to supply control electronics and actuators in industrial environments. Based on a brief study of the electromagnetic relations in the air gap and the solid steel secondary, a power scaling law as function of the geometric parameters and stator current is derived. The scaling law is verified with two-dimensional Finite Element Method (2-D FEM) simulations and measurements on a test setup. The proposed scaling law is an effective tool for estimating the performance of a SLIM for contactless energy harvesting in emerging industry and consumer applications.

**Index Terms**—Energy harvesting, linear induction machine, solid rotor machine, SLIM, induction machines, inductive power transmission, steel, scaling law.

## NOMENCLATURE

$A_1$	Stator current sheet
$A_{\text{slot}}$	Winding window (per coil side)
$B_2$	Secondary flux density
$B_g$	Air gap flux density
$E_g$	Stored energy in air gap
$\delta_{\text{Fe}}$	Secondary skin depth
$\delta_g$	Air gap offset
$g$	Air gap, ideal
$g_m$	Air gap, measured
$I_1, i_1$	Stator phase current (RMS, $i(t)$ )
$I_2, i_2$	Secondary current (RMS, $i(t)$ )
$I_m, i_m$	Main inductance current (RMS, $i(t)$ )
$j_2$	Secondary current density
$j$	Imaginary unit $\sqrt{-1}$
$k$	Power scaling factor
$k_f$	Copper filling factor
$\kappa_{\text{Cu}}$	Copper conductivity
$\kappa_{\text{Fe}}$	Secondary conductivity
$l_y$	Stator width
$l_{\text{end}}$	End winding length
$L_1$	Stator stray inductance
$L'_2$	Secondary stray inductance
$L_m$	Main inductance
$m$	Number of phases
$\mu_{\text{Fe}}$	Secondary apparent permeability

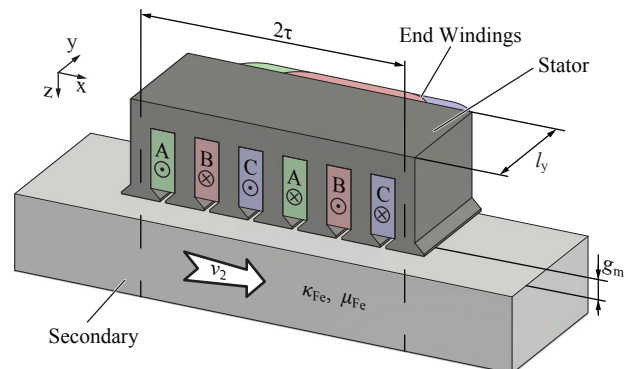


Fig. 1: Scheme of the analyzed and tested SLIM prototype for energy harvesting. The three-phase winding system on the stator is implemented with a distributed one-layer winding.

$N$	Number of turns
$p$	Number of pole pairs
$P_1$	Primary electrical power (RMS)
$P_2$	Secondary extracted electrical power (RMS)
$P_{\text{cu}}$	Stator copper losses (RMS)
$R_1$	Stator winding resistance
$R'_2$	Secondary resistance
$s$	Slip
$\tau$	Pole pitch
$u_1$	Stator phase voltage
$u_m$	Main inductance voltage
$v_2$	Secondary surface speed
$\xi$	Winding factor
$Z'_2$	Secondary impedance
$\omega_1$	Stator angular frequency
$\omega_2$	Secondary angular frequency

## I. INTRODUCTION

Linear Induction Machines (LIMs) [1] and Single-Sided Linear Induction Machines (SLIMs) have been analyzed and tested intensively as prime movers for medium and high power (kW-range) applications such as linear drives for production machines [2], for flywheel energy storages [3], in transportation for levitating [4–6] and self-propelled trains (linear metro) [7, 8]. LIMs and SLIMs are particularly suitable for harsh environments such as high temperatures and dirty or abrasive surrounding conditions since use of permanent

magnets is omitted. Previous studies focused generally on the utilization of LIMs and SLIMs as drives; and therein derived models are tuned for describing thrust generation and electrical behavior at the machine terminals for motoring mode. Nevertheless, favorable properties of SLIMs, such as robust structure and reduced part count make them a viable option also for emerging energy harvesting applications. Therefore, this paper investigates the use of a SLIM for watt-range energy harvesting from a moving steel body with a smooth surface (solid steel secondary). Moreover, a power scaling law is derived based on an ideal machine and verified with experiments and 2-D FEM simulations. The provided scaling law allows to estimate the feasibility of a SLIM-based energy harvesting application in a computationally efficient way.

### A. Principle of Operation

The SLIM topology analyzed in this work is different from a standard rotating induction machine due to its linear stator and its counterpart (secondary), which is a solid (unlaminated) conductive body. However, the underlying principle of operation is conserved. A moving magnetic field induced by the windings in the stator is the anchor point for building up of force and electromechanical energy conversion.

Currents are induced in a conductive body (secondary), when it is permeated by the moving stator field (generated by the stator windings). Lorentz force is built up due to the interaction of the eddy currents and the stator field, which establishes the said electromechanical energy conversion.

### B. Secondary Side Material

In widely used rotating squirrel-cage induction machines, the secondary is a rotor, where the magnetic flux is guided by laminated iron and the induced currents are conducted by dedicated bars of aluminum or copper. However, in solid-secondary (also solid-rotor) machines (cf. Fig. 1), the solid, conductive and ferromagnetic secondary implements both the flux guide and the conductive path for the induced current. In such a system, the electromagnetic properties of the secondary could be enhanced with modifications on the secondary geometry. Axial slitting and/or coating with a highly conductive material such as copper [9, 10] would provide low-impedance paths for eddy currents and improve the electromechanical power conversion.

However, unlike many earlier studies about solid-secondary machines, the analysis shown in this paper focuses on a solid, non-adapted steel secondary with a smooth surface such that the SLIM-type energy harvester is applicable for power extraction from any steel body/surface moving with sufficient speed. Therefore, the presented analysis takes the moving steel secondary as given and does not consider manipulations such as coating or slitting.

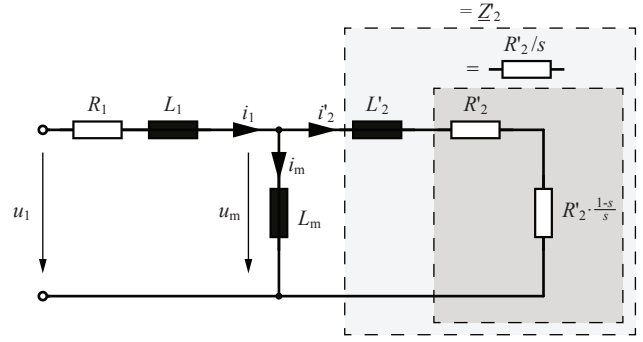


Fig. 2: Induction machine equivalent circuit which is used in the modeling. Index 1 indicates stator-related elements,  $L_m$  is the main inductance and index 2 indicates the secondary-related elements.

## II. SYSTEM OVERVIEW AND MODELING

The well-known induction machine single-phase equivalent circuit shown in Fig. 2 is used for modeling the SLIM under consideration, wherein for convenience, all quantities are related to the stator and the transformed secondary quantities are indicated with an apostrophe ( $'$ ). In the following sections, the equivalent circuit elements of Fig. 2 are considered and expressed as a function of geometry and material parameters.

### A. Stator Modeling

The stator-related circuit elements  $R_1$  and  $L_1$  can be estimated similarly to rotating machine analysis. The stator coil resistance  $R_1$  is defined by the copper wire length and wire cross section, since skin and proximity effects can be neglected for the fundamental frequency range. For the analyzed machine with a distributed one-layer winding with one coil side per phase,  $R_1$  is given as

$$R_1 = p N^2 \frac{2(\tau + l_y + l_{\text{end}})}{\kappa_{\text{Cu}} A_{\text{slot}} k_f}, \quad (1)$$

where  $l_{\text{end}}$  accounts for the end winding length. As it will be shown in more detail later,  $R_1$  plays a significant role concerning the machine efficiency. A too high  $R_1$  leads to high losses in the stator windings and consequently prevents any electrical power to be harvested by the machine.

The primary stray inductance  $L_1$  can be obtained with an analytic stray path calculation [11], an FEM simulation or with measurement on a manufactured stator. The primary stray inductance causes inductive voltage drop; however, since the energy harvester is driven with constant current amplitude, the effect of  $L_1$  on harvested power is negligible. Moreover, the stator of the built SLIM prototype for energy harvesting is designed such that core losses can be neglected for this study.

### B. Modeling of Main and Secondary Impedances

Unlike to the modeling of stator related elements ( $R_1$  and  $L_1$ ), the analysis of the magnetic fields in the air gap and secondary

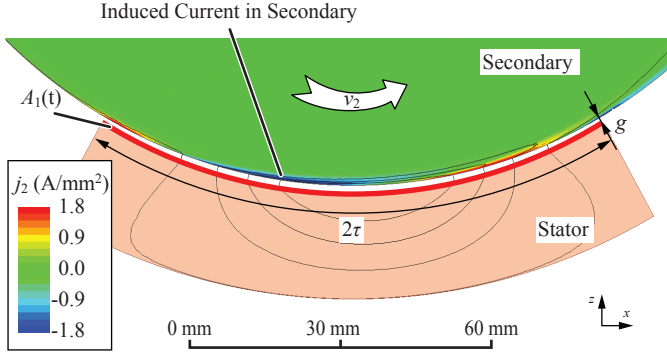


Fig. 3: FEM simulation of SLIM for energy harvesting. The system is modeled two-dimensionally in the  $x$ - $z$  plane and stator excitation is lumped in a current sheet. Moreover, the SLIM is modeled as a bent around a small sector of a secondary wheel and the current in the secondary  $j_2$  is mainly induced in a small skin depth  $\delta_{\text{Fe}}$  facing the stator, justifying the modifications for confirming the scaling law with FEM.

is a more complex task. It is based on induction of currents in the solid, smooth secondary material.

As an outcome of the analysis presented in Appendix A and conducted for an ideal machine, which is endlessly extended (in  $x$ - and  $y$ -direction cf. Fig. 1) and assumes linear secondary material (constant magnetic permeability), the main inductance  $L_m$ , the secondary stray inductance  $L'_2$  and the secondary resistance  $R'_2$  can be expressed as

$$\begin{aligned} L_m &= \frac{2}{\pi^2} m p (N\xi)^2 \mu_0 \cdot \frac{l_y \tau}{g}, \\ L'_2 &= m p (N\xi)^2 \mu_{\text{Fe}} \cdot \frac{l_y \delta_{\text{Fe}}}{\tau}, \\ R'_2 &= 2 m p (N\xi)^2 \cdot \frac{l_y}{\kappa_{\text{Fe}} \delta_{\text{Fe}} \tau}. \end{aligned} \quad (2)$$

### C. FEM Analysis

An FEM analysis gives insight into the operating principle and is required to confirm the derived relations for different pole pitch values  $\tau$ , where measurements on a physical system would require various stators to be manufactured. The SLIM is modeled two-dimensionally in the  $x$ - $z$  plane (cf. Fig. 3), where the stator is bent around a small sector of a secondary wheel and the resulting topology is also called sector motor in [12]. The modification can be justified with the results of the FEM simulation depicted in Fig. 3, since the current in the secondary  $j_2$  is mainly induced in a small skin depth  $\delta_{\text{Fe}}$  and curvature of the secondary does not significantly affect the performance of the analyzed system. Additionally, the eddy currents in the incoming secondary matter have sufficiently vanished as it can be noted on the left side of the secondary (cf. Fig. 3). Moreover, the excitation due to stator windings is lumped in a time-dependent current sheet on the stator surface.

These simplifications allow a computationally-efficient analysis of the system and confirmation of the scaling law, while

performance-distinguishing elements as the air gap flux and the secondary current distribution are modeled accurately. A time-transient simulation is conducted with a moving secondary mesh and only the solution after the system reaches steady-state is considered. A method for accounting the finite width in  $y$ -direction, while the system is analyzed with 2-D FEM in the  $x$ - $z$  plane is proposed in [12]. Nevertheless, nonideal effects in  $y$ -direction influence, but do not dominate the machine's behavior in an energy harvesting application.

## III. SCALING LAW FOR ENERGY HARVESTING

As stated in Sec. II-B, the equivalent circuit elements for main inductance  $L_m$  and secondary ( $L'_2$  and  $R'_2$ ) are derived for an ideal machine. However, in literature, nonideal effects due to finite length in  $x$ -direction (longitudinal end effect) [13] and finite width in  $y$ -direction (transversal edge effect) [14] of the LIM as well as effects caused by saturation [15] in the solid iron/steel secondary are described. Those effects can be identified as challenges for an accurate modeling due to the complexity and the bounded validity of correction factors proposed in literature. Therefore, this paper proposes and verifies that the power scaling analysis for a SLIM energy harvester can be derived from the analysis of said ideal machine while all nonideal effects are taken into account by a lumped scaling factor  $k$ .

Firstly, in Appendix B, the electric power extracted from the secondary  $P_2$  can be expressed as a function of slip  $s$ , magnetizing current  $I_m$ , secondary speed  $v_2$ , geometric parameters and secondary material properties  $\kappa_{\text{Fe}}$  and  $\mu_{\text{Fe}}$ . The expression of  $P_2$  and its scaling for the ideal machine is derived as

$$P_2 \propto (N \xi I_m)^2 v_2^{3/2} \frac{l_y \tau^{3/2}}{g^2} \sqrt{\frac{\kappa_{\text{Fe}}}{\mu_{\text{Fe}}}}. \quad (3)$$

Specifically, this relation allows to predict the performance of a SLIM accurately when scaled with data from few measurements or FEM simulations. Beneficially, as confirmed in Sec. IV-B, nonideal effects and losses in the system, except for primary copper losses, scale with the extracted power from the secondary  $P_2$ . Since the primary current  $I_1$  is proportional to the main inductance current  $I_m$ , the extracted electrical power on the primary  $P_1$  can be expressed conveniently as

$$P_1 \approx \underbrace{-k \cdot (N \xi I_1)^2 v_2^{3/2} \frac{l_y \tau^{3/2}}{g^2}}_{P_2} + \underbrace{m R_1 I_1^2}_{P_{\text{cu}}}. \quad (4)$$

The power scaling factor  $k$ , estimated by at least a single measurement or FEM analysis, allows to accumulate all nonideal effects, which make an actual SLIM harvester differ from the analyzed ideal machine. Clearly, this leads to a time-efficient and sufficiently accurate analysis of the complex relations in the system.

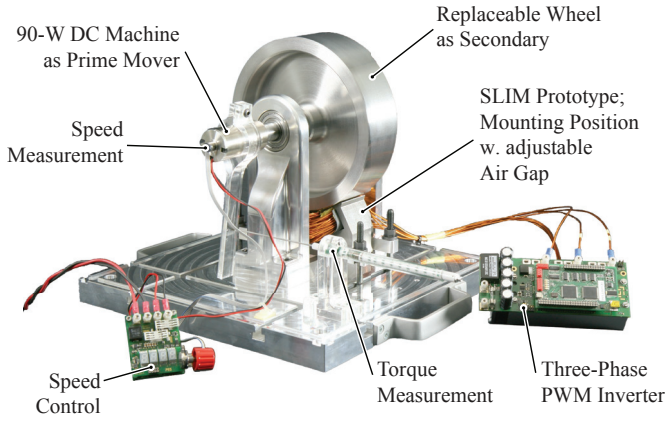


Fig. 4: Test setup with mounted SLIM energy harvester. A 90-W DC machine drives the secondary wheel and the secondary surface speed  $v_2$  is set. The SLIM stator is bent around a small sector ( $60^\circ$ ) of the secondary wheel and mounted on the base plate. The air gap can be adjusted precisely with spacers between base plate and stator. The stator is driven by a current controlled PWM inverter.

TABLE I: Parameters of test setup for experimental results.

Parameter	Variable	Value
Pole pitch	$\tau$	52 mm
Stator width	$l_y$	45 mm
Number of pole pairs	$p$	1
Number of phases	$m$	3
Winding window (per coil side)	$A_{\text{slot}}$	267 mm <sup>2</sup>
Measured air gap	$g_m$	0.4...20 mm
Stator material		M235-35A
Secondary material		Steel C45E
Secondary conductivity	$\kappa_{\text{Fe}}$	6.17 MS/m
Secondary apparent permeability (considering partial saturation)	$\mu_{\text{Fe}}$	500 $\mu_0$
Secondary surface speed	$v_2$	0...50 m/s
Copper filling factor	$k_f$	0.234
Number of turns	$N$	30
Wire gauge		AWG 14
Winding factor	$\xi$	0.955
Stator winding resistance <sup>a</sup>	$R_1$	81 m $\Omega$
Stator stray inductance <sup>a</sup>	$L_1$	460 $\mu\text{H}$
Air gap offset	$\delta_g$	0.4 mm
Nominal measurement parameters		
Stator phase current (RMS)	$I_1$	2 A
Secondary surface speed	$v_2$	22.2 m/s
Slip	$s$	-1.12
Measured air gap	$g_m$	1 mm

<sup>a</sup> Measured at 50 Hz; mean value for three phases.

#### IV. EXPERIMENTAL SETUP AND MODEL VERIFICATION

In order to verify the described modeling approach, the test setup depicted in Fig. 4 is designed and built. As described for the FEM model in Sec. II-C, the linear secondary is also

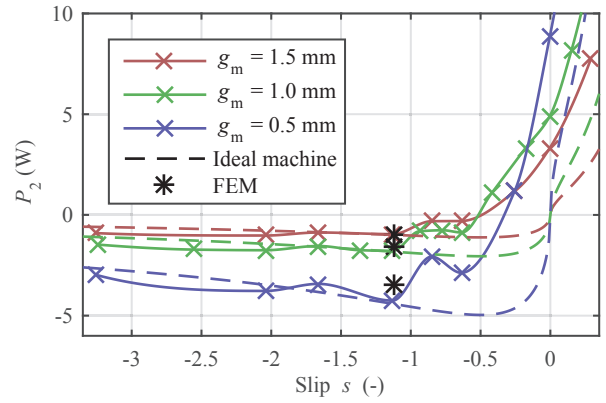


Fig. 5: Extracted power  $P_2$  over slip at different air gap values, illustrating the power extraction from the secondary. Solid lines show measurements and the dashed lines show the results obtained for the ideal machine (cf. (24)).  $P_2$  as shown is measured  $P_1$ , subtracted by the calculated copper losses  $P_{\text{cu}}$ . For  $I_1$  and  $v_2$ , the nominal measurement parameters according to Table I apply. Due to the finite length of the machine, the measured power curve shows several local minima and deviates from a curve derived for the ideal machine.

replaced by a wheel in the test setup and the SLIM is bent around a small sector ( $60^\circ$ ) of the secondary wheel, to emulate the linear machine geometry. Table I summarizes the key parameters of the SLIM prototype. Measurements over a range in slip  $s$ , measured air gap  $g_m$ , secondary surface speed  $v_2$  and primary current  $I_1$  are presented in the following.

The SLIM under test is mounted under the secondary wheel which can be replaced in order to test the machine performance with different secondary materials and geometries. This setup also allows to vary the air gap of the system precisely and provides a mechanically stiff mounting. The SLIM is electrically driven with a three-phase current controlled PWM inverter which can be seen on the right side of Fig. 4. An interface to a control PC allows to set phase current amplitude and frequency of the SLIM. All phase currents and phase-to-star point voltages are measured with a precision power analyzer Yokogawa WT3000 to obtain  $P_1$ . The secondary is mechanically driven by a 90-W DC machine which is supplied by a speed control electronics. The reaction torque on the prime mover is measured by a lever and a spring force sensor.

##### A. Scaling Factor $k$ and Influence of Slip

In Fig. 5, the characteristic of extracted power  $P_2$  over slip is shown. The slip definition is similar to rotating induction machine convention and can be expressed as a function of electrical stator angular frequency  $\omega_1$ , secondary surface speed  $v_2$  and pole pitch  $\tau$ .

$$s = 1 - \frac{\pi/\tau v_2}{\omega_1} \quad (5)$$

In the region  $-2 < s < 0.5$ , significant power is harvested. Due to nonideal effects caused by the finite length and width of the machine, the measured power curve shows several

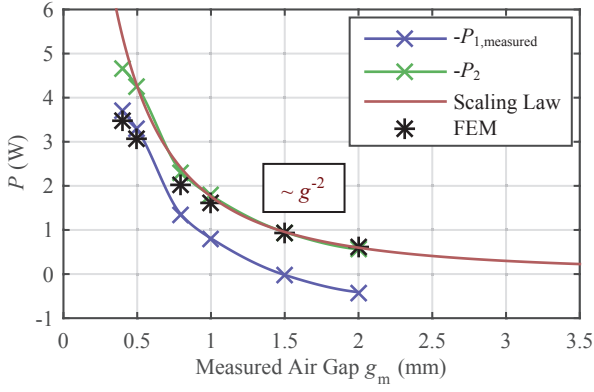


Fig. 6: Investigation of the air gap influence and comparison with the scaling law. For  $I_1$  and  $v_2$  and  $s$  the nominal measurement parameters according to Table I apply. Air gap can be identified as a key parameter for the use of a single-sided SLIM for energy harvesting.

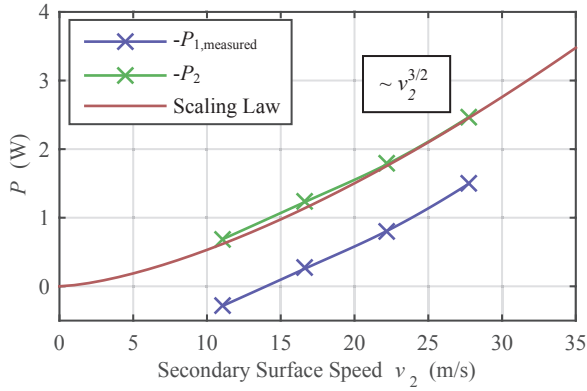


Fig. 7: Investigation of the secondary surface speed influence and comparison with the scaling law. For  $I_1$ ,  $g_m$  and  $s$  the nominal measurement parameters according to Table I apply.

local minima and deviates from a curve derived for the ideal machine (cf. (24)). However, according to the measurements and 2-D FEM simulations, the slip where maximal power is extracted (minimum  $P_2$ ), is independent of measured air gap  $g_m$ , secondary surface speed  $v_2$  and stator phase current  $I_1$ . For the harvester at hand, this point is identified as  $s_{opt} = -1.12$ .

The data obtained from the point with optimal slip is the initialization point for the proposed scaling law (4). The power scaling factor  $k$  is obtained as the least squares fit for data of three different air gap values  $g_m \in \{0.5 \text{ mm}, 1.0 \text{ mm}, 1.5 \text{ mm}\}$  as

$$k_{\text{measured}} = 1.90 \cdot 10^{-8} \Omega \frac{\text{s}^{3/2}}{\text{m}^{5/2}}.$$

Moreover, the air gap  $g$  applied in the scaling law is adjusted by an offset for

- compensating degradation due to laser cutting of the stator iron, as analyzed in [16],
- slotting effect (instead of Carter factor) and
- a positive offset due to curvature mismatch, when the

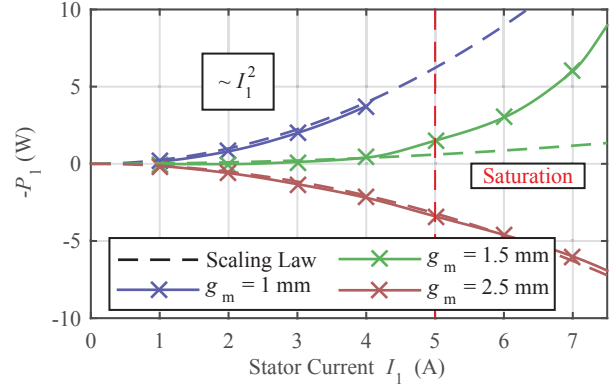


Fig. 8: Investigation of stator current  $I_1$  influence for different air gap values. For  $v_2$  and  $s$  the nominal measurement parameters according to Table I apply. With too high air gap values ( $g_m > 1.5 \text{ mm}$ ) it was not possible to harvest power and with  $I_1 > 5 \text{ A}$ , saturation effects on the secondary occur.

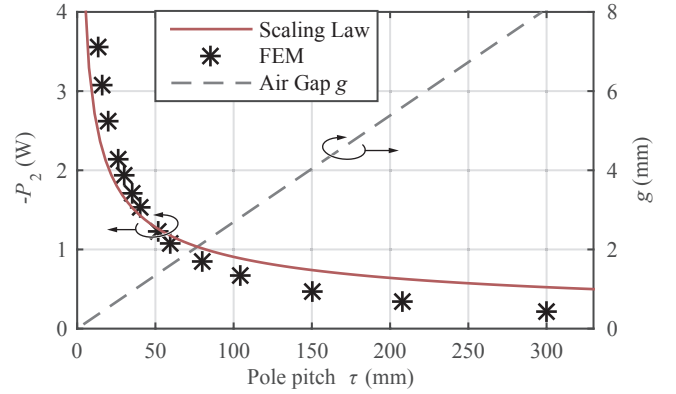


Fig. 9: Simulation results of electrical power over pole pitch  $\tau$ , where the ratio  $\tau/g$  is kept constant such that similar relations of impedances are given.

stator, designed for  $g_m = 1.5 \text{ mm}$  is mounted with smaller air gap.

Therefore,

$$g = g_m + \delta_g \quad (6)$$

with  $\delta_g = 0.4 \text{ mm}$  is applied in the scaling law and  $g_m$  is the measured air gap.

### B. Verification of the Scaling Law

Fig. 6 plots extracted power versus air gap and compares measurements with the scaling law. Over the measured air gap range  $0.4 \text{ mm} \leq g_m \leq 2 \text{ mm}$ , the measurements perfectly confirm the predicted power scaling  $P_2 \propto g^{-2}$ , which can be explained qualitatively with the  $L_m \propto g^{-1}$  scaling of the magnetization inductance.

2-D FEM simulation results show a slight mismatch to both the measurements and the scaling law for small air gap. The large aspect ratio, namely high  $\tau/g$  ratio, is a challenge for the discretization (meshing) and a possible cause for the mismatch.

Also the power scaling over secondary surface speed can be confirmed as clearly depicted in Fig. 7. The scaling  $P_2 \propto v_2^{3/2}$  results from the positive effect of increasing electric system frequency which is partly canceled by the negative effect of increasing secondary impedance due to reduced skin depth.

In Fig. 8, the  $P_1$  over  $I_1$  measurements are given for different air gap values and the scaling  $P_1 \propto I_1^2$  can be confirmed for  $I_1 < 5$  A. Further insight in the usage of SLIM for energy harvesting can be obtained concerning the influence of  $R_1$  on the system. A region  $g_m < 1.5$  mm, which allows energy harvesting, and a region  $g_m > 1.5$  mm, where energy harvesting is impossible, can be identified. For large air gap values, the copper losses  $P_{cu}$  due to  $R_1$  are simply higher than the harvested power  $P_2$  and increasing the current does not lead to higher power extraction, since both  $P_2$  and  $P_{cu}$  scale with  $I_1^2$ .

It can be seen that the given scaling law is valid for the region  $I_1 < 5$  A since it relies on nonsaturated secondary material. Saturation indeed improves the extraction of  $P_2$ . On the other hand, for typical watt-range energy harvesting applications, nonsaturated secondary material can be assumed since an apparent power of  $S_1 > 100$  VA is required for saturation with the test setup considered here and  $g_m = 1.5$  mm.

The power to pole pitch relation is analyzed with 2-D FEM simulations and depicted in Fig. 9 and the analysis of the pole pitch influence shows a boundary for the validity of the scaling law (4). It holds with reasonable accuracy when the aspect ratio  $\tau/g$  is kept approximately constant and following effects limit the validity when deviating from the stated aspect ratio widely.

- When the aspect ratio becomes too small  $\tau/g \ll 25$ , which means large air gap, more and more flux lines close in the air gap without entering the secondary, resulting in lower inductive coupling than predicted.
- When the aspect ratio becomes too large  $\tau/g \gg 130$ , the secondary impedance becomes large compared to the magnetization impedance. Accordingly, the harvested power is limited.

## V. CONCLUSION

This paper discusses the application of a Single-Sided Linear Induction Machine (SLIM) with solid steel secondary employing a smooth surface for energy harvesting. A test setup is built and a power of  $P_1 \approx -4$  W is extracted on the machine terminals, when maintaining an air gap of  $g_m = 1$  mm and a secondary speed of  $v_2 = 22.2$  m/s. A scaling law, which relates the geometric parameters to the extracted power is derived and confirmed with measurements and 2-D FEM simulations. The scaling law is valid for typical energy harvesting conditions, namely a comparably large pole pitch to air gap ratio ( $25 < \tau/g < 130$ ) and nonsaturated secondary material. With the use of the this scaling law and a power scaling factor  $k$ , which can be estimated by few measurements or FEM simulations, the complex relations in a SLIM energy

harvesting system can be analyzed in an accurate and highly time-efficient way.

Energy harvesting with a SLIM from a moving steel body is particularly suitable for harsh environments such as high temperatures and dirty or abrasive surrounding conditions since use of permanent magnets is omitted. On the other hand, as a practical limitation for the use of the described energy harvester, the need for an external system startup, similar to generator startup of an induction machine, should be mentioned. The provided analysis and the conducted measurements show that the analyzed concept is suitable for watt-range energy harvesting with secondary surface speed  $v_2 > 15$  m/s and air gap  $g_m < 1$  mm. Concepts capable of harvesting over larger air gap at the expense of reduced robustness are currently under investigation [17].

## VI. ACKNOWLEDGMENT

The authors would like to express their sincere appreciation to Nabtesco Corp., Japan, for the financial and technical support of research on energy harvesting technologies at the Power Electronic Systems Laboratory, ETH Zurich, which provided the basis for achieving the results presented in this paper. In particular, inspiring technical discussions with K. Nakamura and Y. Tsukada should be acknowledged. Furthermore, acknowledgment is given to L. Gasser who contributed to the inverter design and conducted initial measurements in the course of his M.Sc. thesis. Moreover, the authors acknowledge the support of CADFEM (Suisse) AG concerning the ANSYS software.

## APPENDIX A EQUIVALENT CIRCUIT

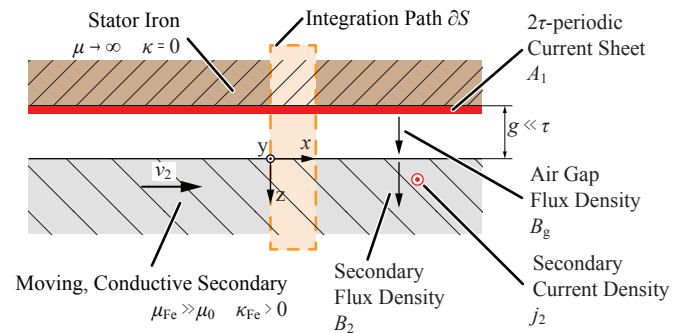


Fig. 10: Simplified 2-D model of the ideal SLIM with solid steel secondary.

In the following, the elements of the equivalent circuit are derived for the ideal machine. Fig. 10 illustrates the geometry and symbols used for the derivation. Moreover, the relation between secondary frequency, slip and stator frequency is

$$\omega_2 = s \omega_1 . \quad (7)$$

The flux density in the air gap can be assumed as

$$\vec{B}_g(t) = \begin{pmatrix} B_{g,x} \\ B_{g,z} \end{pmatrix} = \begin{pmatrix} 0 \\ \hat{B}_g \cdot \sin(\pi/\tau x + \omega_1 t) \end{pmatrix} \quad (8)$$

and the following equation, derived from Maxwell's equations must hold in the secondary matter:

$$\nabla \times (\nabla \times \vec{B}_2) = -\mu_{Fe} \cdot \kappa_{Fe} \cdot \frac{\partial \vec{B}_2}{\partial t}. \quad (9)$$

With benefit one can define the flux density in the secondary  $\vec{B}_2$  as the real part of an exponential function with complex eigenvalue  $\underline{s}_B$

$$\vec{B}_2(t) = \text{Re} \left\{ \underline{\vec{B}}_2 \cdot \exp \left( \underline{s}_B^T \cdot \begin{pmatrix} x \\ z \\ t \end{pmatrix} \right) \right\}. \quad (10)$$

With the structure defined in (10), one can derive a solution for (9), where (8) is the boundary condition for the interface between air gap and secondary. With the reasonable assumption that the pole pitch  $\tau$  is sufficiently larger than the secondary skin depth  $\delta_{Fe}$ , one can obtain the complex eigenvalue  $\underline{s}_B$  of the field problem as

$$\underline{s}_B = \begin{pmatrix} j\pi/\tau \\ -(1+j)/\delta_{Fe} \\ j\omega_1 \end{pmatrix}, \quad \delta_{Fe} = \sqrt{\frac{2}{|\omega_2| \cdot \mu_{Fe} \cdot \kappa_{Fe}}}. \quad (11)$$

Therefore, the amplitude of the field distribution in the secondary  $\underline{\vec{B}}_2$  can be obtained as

$$\underline{\vec{B}}_2 = \hat{B}_g \cdot \begin{pmatrix} -(1+j)/\delta_{Fe} \cdot \pi/\tau \\ -j \end{pmatrix}. \quad (12)$$

Furthermore, the current distribution in the secondary  $j_2$  can be found as

$$j_2 = \text{Re} \left\{ -\frac{\hat{B}_g \pi}{\mu_{Fe} \tau} \cdot \exp \left( \underline{s}_B^T \cdot \begin{pmatrix} x \\ z \\ t \end{pmatrix} \right) \right\}. \quad (13)$$

By applying Ampere's law

$$\oint \frac{\vec{B}}{\mu} d\vec{s} = \int j ds, \quad (14)$$

one can obtain the stator current sheet as

$$A_1(t) = \text{Re} \left\{ \hat{A}_1 \cdot \exp \left( (j\pi/\tau \quad j\omega) \begin{pmatrix} x \\ t \end{pmatrix} \right) \right\} \\ \hat{A}_1 = \underbrace{\hat{B}_g \frac{g \pi}{\mu_0 \tau}}_{\hat{A}_m} + \underbrace{\hat{B}_g \frac{\tau (1+j)}{\mu_{Fe} \delta_{Fe} \pi}}_{\hat{A}_2}. \quad (15)$$

The terms in the current sheet can be interpreted with a simple thought experiment. Assuming a vanishing air gap  $g \rightarrow 0$ , the current through the main inductance in the equivalent circuit  $i_m$  must similarly vanish. Since the current sheet is generated by current  $i_1$ , a separation into a fraction dedicated for the magnetization in the air gap  $\hat{A}_m$  and a fraction which is transformed to the secondary  $\hat{A}_2$  can be conducted in (15). Given that the current sheet is the fundamental of a current  $i_1$

in a  $m$ -phase winding in the primary, where the flux vector of the first winding is located at  $x = 0$ , following relation for the primary current space vector holds

$$\underline{i}_1(t) = -j \underbrace{\frac{\hat{A}_1 \tau}{m N \xi}}_{\hat{i}} \exp(j\omega_1 t). \quad (16)$$

With the balance of stored energy in the air gap,

$$E_g(t) = \frac{m}{2} L_m \frac{i_m(t) \cdot i_m^*(t)}{2} = \int_0^{2\tau} \frac{\|\vec{B}_g(t)\|^2}{2\mu_0} l_y p g dx \quad (17)$$

one can express the main inductance as

$$L_m = \frac{2}{\pi^2} m p (N\xi)^2 \mu_0 \cdot \frac{l_y \tau}{g}. \quad (18)$$

With a similar balance of stored energy in the secondary, one can find the secondary stray inductance as

$$L'_2 = m p (N\xi)^2 \mu_{Fe} \cdot \frac{l_y \delta_{Fe}}{\tau}. \quad (19)$$

It is clear from (15) (due to the  $1+j$  factor) that the phase angle in current sheet fraction dedicated for power transfer to the secondary  $\hat{A}_2$  is  $+45^\circ$  for linear material, as firstly published in [18]. Due to the suitable definition of the coordinate system, it is equal to the phase angle between main inductance voltage  $u_m$  and secondary current  $i'_2$ . Therefore, for the secondary resistance the following can be obtained

$$|\omega_1 L'_2| = |R'_2/s|, \quad (20)$$

$$R'_2 = 2 m p (N\xi)^2 \cdot \frac{l_y}{\kappa_{Fe} \delta_{Fe} \tau}. \quad (21)$$

## APPENDIX B POWER IN THE SECONDARY

With the obtained equivalent circuit elements, the secondary impedance  $Z'_2$  can be rewritten as

$$Z'_2 = j\omega_1 L'_2 + R'_2/s \\ Z'_2 = \sqrt{2} (j + \text{sgn}(s)) \frac{\omega_1}{\sqrt{|\omega_2|}} m p (N\xi)^2 \frac{l_y}{\tau} \sqrt{\frac{\mu_{Fe}}{\kappa_{Fe}}}. \quad (22)$$

The extracted power in the secondary  $P_2$  can be expressed with the voltage across the main inductance  $\underline{u}_m = j\omega_1 L_m \underline{i}_m$  as

$$P_2 = \text{Re} \left\{ \frac{m}{2} \frac{\underline{u}_m \cdot \underline{u}_m^*}{Z_2'^*} \right\} \\ P_2 = \text{sgn}(s) \frac{\sqrt{2} \mu_0^2}{\pi^4} \omega_1 \sqrt{|\omega_2|} \\ p (m N \xi |i_m|)^2 \frac{l_y \tau^3}{g^2} \sqrt{\frac{\kappa_{Fe}}{\mu_{Fe}}}. \quad (23)$$

With the RMS value of the current sheet  $I_m = 1/\sqrt{2} |i_m|$ ,  $P_2$  can be rewritten as a function of geometric parameters, secondary material parameters, slip  $s$ , secondary surface speed  $v_2$  and winding parameters, defining the current sheet, the

power scaling can be expressed as

$$P_2 = \text{sgn}(\omega_1 s) \sqrt{\left| \frac{s}{(1-s)^3} \right|} \frac{\mu_0^2}{\sqrt{2} \pi^{5/2}} \quad (24)$$

$$p (mN\xi I_m)^2 v_2^{3/2} \frac{l_y \tau^{3/2}}{g^2} \sqrt{\frac{\kappa_{Fe}}{\mu_{Fe}}}$$

and

$$P_2 \propto (N \xi I_m)^2 v_2^{3/2} \frac{l_y \tau^{3/2}}{g^2} \sqrt{\frac{\kappa_{Fe}}{\mu_{Fe}}}.$$

#### REFERENCES

- [1] W. Xu, J. G. Zhu, Y. Zhang, Z. Li, Y. Li, Y. Wang, Y. Guo, and Y. Li, "Equivalent circuits for single-sided linear induction motors," *IEEE Transactions on Industry Applications*, vol. 46, no. 6, pp. 2410–2423, September 2010.
- [2] J. F. Gieras, *Linear induction drives*. Oxford University Press, 1994.
- [3] E. Bolte, "Dreidimensionale Berechnung des asynchronen Sektormotors mit massiveisernem Rotor (in German)," Ph.D. dissertation, Universität Dortmund, 1979.
- [4] J. Stickler, "A study of single-sided linear induction motor performance with solid iron secondaries," *IEEE Transactions on Vehicular Technology*, vol. 31, no. 2, pp. 107–112, May 1982.
- [5] Y. Yasuda, M. Fujino, M. Tanaka, and S. Ishimoto, "The first HSST maglev commercial train in Japan," *Proceedings of the International Conference on Magnetically Levitated Systems and Linear Drives (MAGLEV)*, pp. 76–85, October 2004.
- [6] Y. Nozaki, T. Koseki, and E. Masada, "Analysis of linear induction motors for HSST and linear metro using finite difference method," *Proceedings of the International Symposium on Linear Drives for Industry Applications (LDIA)*, pp. 168–171, September 2005.
- [7] T. C. Wang, "Linear induction motor for high-speed ground transportation," *IEEE Transactions on Industry and General Applications*, no. 5, pp. 632–642, September 1971.
- [8] W. Xu, J. Zhu, Y. Zhang, D. Dorrell, and Y. Guo, "Electromagnetic optimal design of a linear induction motor in linear metro," *Proceedings of the Annual Conference on IEEE Industrial Electronics Society (IECON)*, pp. 3067–3072, November 2010.
- [9] T. Hupponen, "High-speed solid-rotor induction machine - electromagnetic calculation and design," Ph.D. dissertation, Lappeenranta University of Technology, 2004.
- [10] J. F. Gieras, *Handbook of electric motors*. Marcel Dekker, 2004, ch. 4.6.2.4 Rotors with conductive layers, p. 273.
- [11] V. D. Nene, *Handbook of electric motors*. Marcel Dekker, 2004, ch. 4.5.4.3 Stator slot leakage reactance, pp. 268–269.
- [12] J. Lemmens, W. Deprez, and J. Driesen, "2D finite element analysis of a solid rotor sector motor," *Proceedings of the IEEE Benelux Young Researchers Symposium*, March 2010.
- [13] S. Yamamura, H. Ito, and Y. Ishulawa, "Theories of the linear, induction motor and compensated linear induction motor," *IEEE Transactions on Power Apparatus and Systems*, vol. PAS-91, no. 4, pp. 1700–1710, July 1972.
- [14] H. Bolton, "Transverse edge effect in sheet-rotor induction motors," *Proceedings of the Institution of Electrical Engineers*, vol. 116, no. 5, pp. 725–731, May 1969.
- [15] B. Chalmers and I. Woolley, "General theory of solid-rotor induction machines," *Proceedings of the Institution of Electrical Engineers*, vol. 119, no. 9, pp. 1301–1308, September 1972.
- [16] S. Steentjes, G. von Pfingsten, and K. Hameyer, "An application-oriented approach for consideration of material degradation effects due to cutting on iron losses and magnetizability," *IEEE Transactions on Magnetics*, vol. 50, no. 11, pp. 1–4, November 2014.
- [17] M. Flankl, A. Tüysüz, and J. W. Kolar, "Analysis of a watt-range contactless electromechanical energy harvester facing a moving conductive surface," *Proceedings of the IEEE Energy Conversion Congress and Exposition 2015 (ECCE 2015)*, September 2015, to be published.
- [18] W. Gibbs, "Induction and synchronous motors with unlaminated rotors," *Journal of the Institution of Electrical Engineers-Part II: Power Engineering*, vol. 95, no. 46, pp. 411–420, 1948.